2MAE205 Physics and Modelling of Turbulence

Design Office : RANS Simulations of Turbulent Shear Flows

Mitchell Whyte
Sajeed Hussain SHAIK

15 décembre 2023

Turbulent jet

In this first part, numerical simulations of a free turbulent jet, as represented in figure 1, will be performed. These simulations will be first validated with respect to experimental data provided by NASA. The main turbulent features of the jet will be analysed, followed by an investigation into the influence of the numerical model constants, the boundary conditions, and the choice of turbulent model.

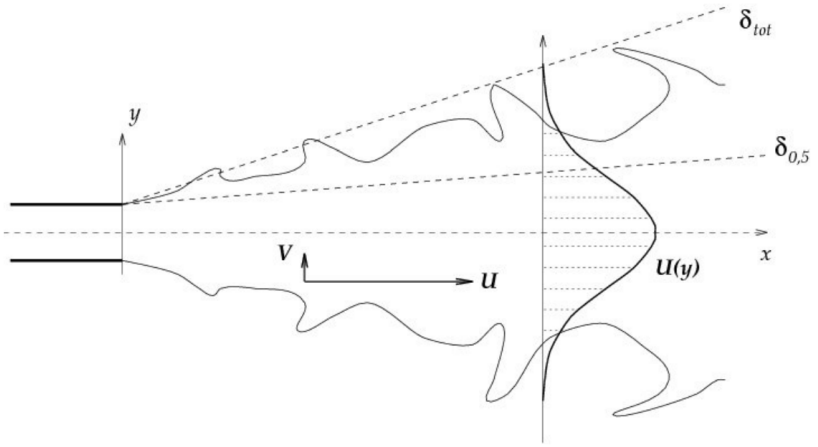

FIGURE 1 – Schematic of cross section view of a fully turbulent jet

The analysis will be initially performed on a round axisymmetric jet of radius $r = 25.4mm$. The ambient pressure is set to $P = 101325Pa$ whereas the nozzle inlet pressure is fixed at $P = 127257Pa$, producing a jet exiting the nozzle with a Mach Number around 0.51. In order to ease the convergence of the simulations a co-flow on the order of Mach number 0.01 is imposed in the ambient region. Based on the jet diameter, D_{jet}, and the experimental conditions the Reynolds number for this flow condition can be calculated to be $Re = 617250$.

The provided computational domain can be seen in figure 2. All lengths are determined in terms of the radius of the jet r. The exit of the nozzle, corresponding to the start of the free jet, was chosen to be situated at $x = 0$.

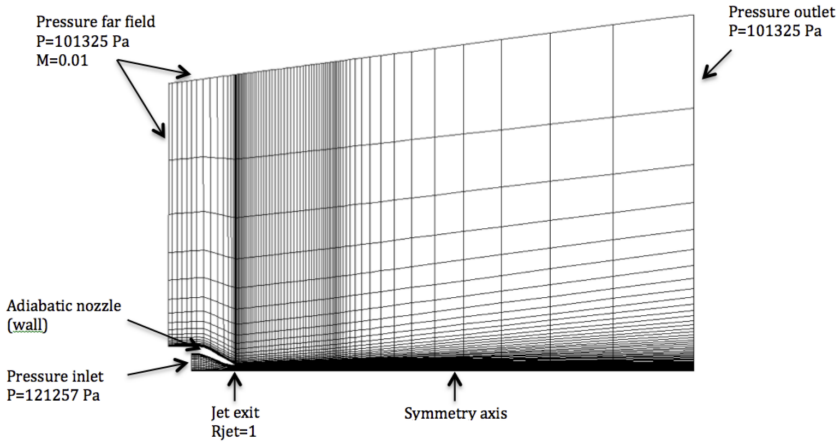

FIGURE 2 – Computational domain used in the simulations of the turbulent free jet

Unless otherwise specified the standard $k - \epsilon$ model is used to model the turbulence of the jet. Like all simulations, convergence must first be evaluated on the basis of the residuals. A representation of the difference between the numerical and analytic solutions, the residuals should tend to zero as the simulation progresses. In this case it can be seen that the residuals reach a stable value after approximately 500 iterations. Though the residuals do not tend to zero, the values are of a sufficiently small magnitude that the simulation can be deemed converged.

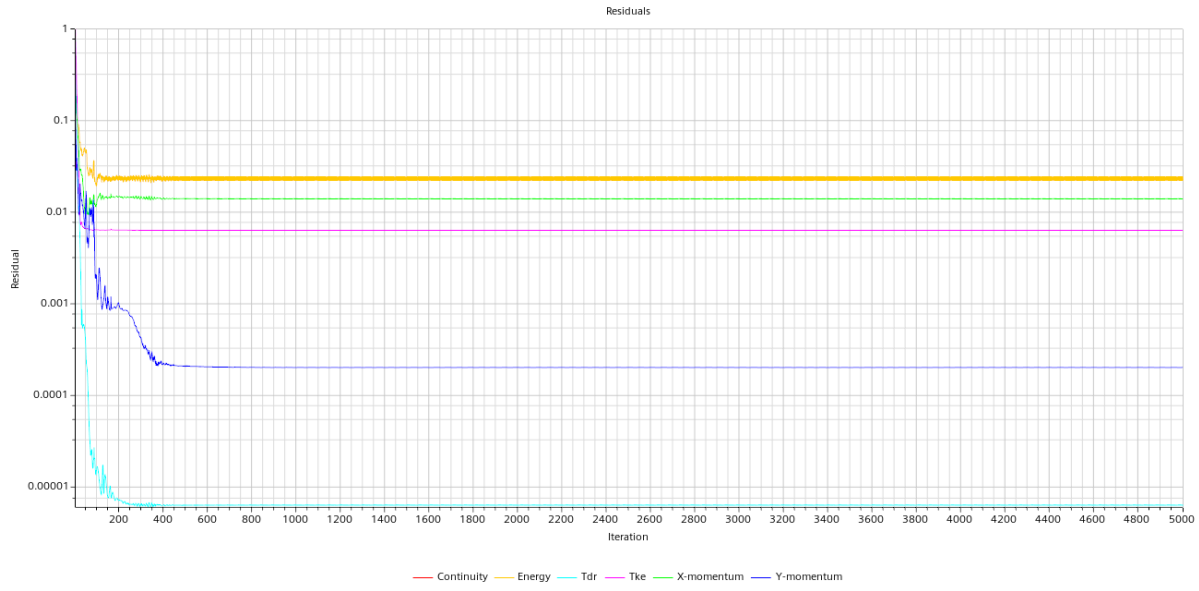

FIGURE 3 – Residuals computed from the initial simulation of the round turbulent jet

The main physical characteristics of the turbulent jet are : the potential core, the

adaptation zone, and the self-similar region. The potential core is the region in which the jet velocity is equal to the velocity at the nozzle exit. The height of the core decreases as the shear layers of the jet grow in size, terminating where the shears layers intersect with the jet axis. figure 4 shows the velocity magnitude through out the jet, as well as the evolution of the velocity along the jet axis.

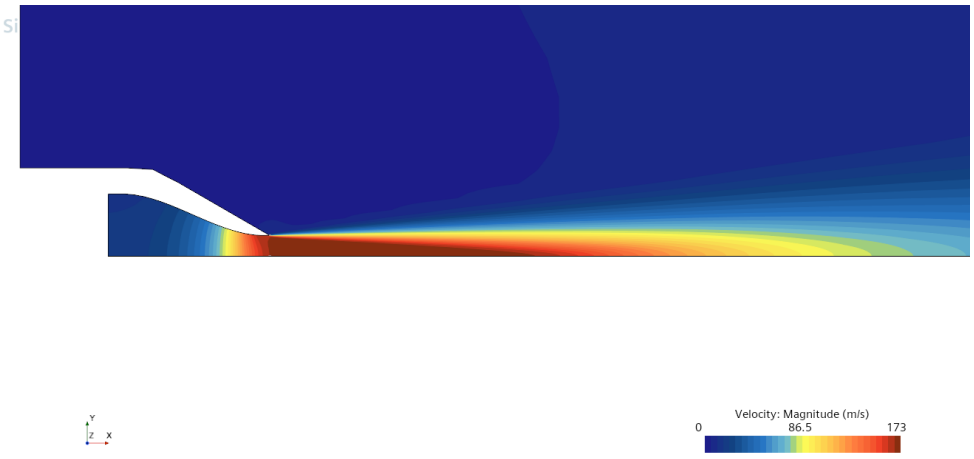

(a)

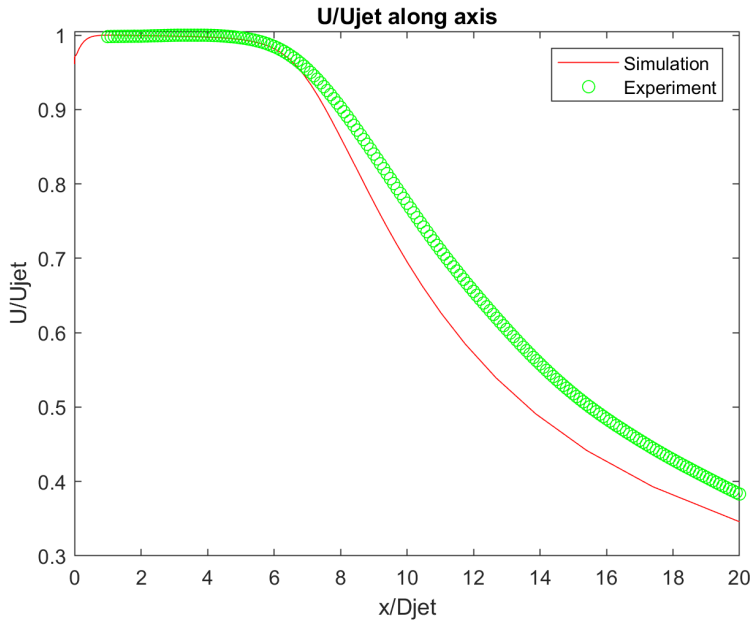

(b)

FIGURE 4 – Velocity of axisymmetric turbulent free jet

In order to determine the length of the potential core from the velocity curve, a threshold

of a 2% velocity decrease was set and used in all subsequent analyses. From this, the potential core was determined to end at approximately $x/D = 6$. This is slightly shorter than the experimental value of $x/D = 6.2$; a variation on the order of 3%, this suggests that the $k - \epsilon$ model can accurately describe the potential core of the jet.

The shear layers have non zero thickness, thus the area over which they intersect the jet axis is known as the adaptation zone. Within this region the maximum turbulent kinetic energy along the axis occurs.

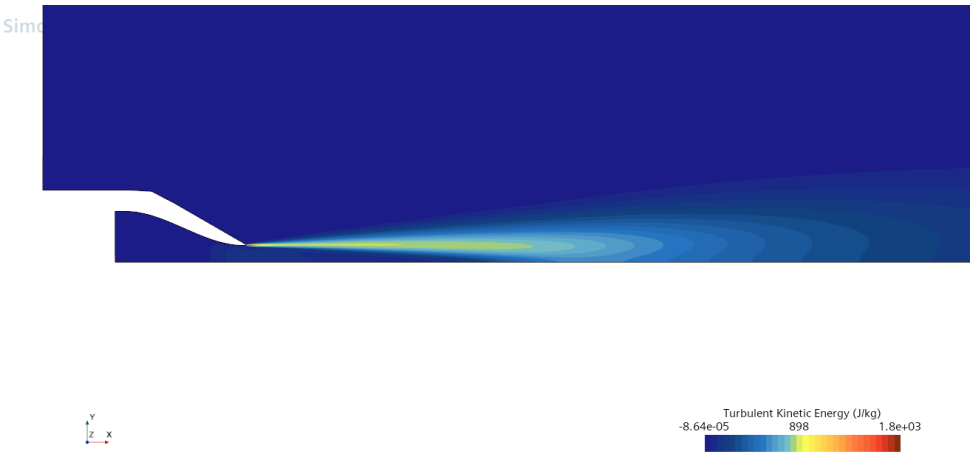

(a)

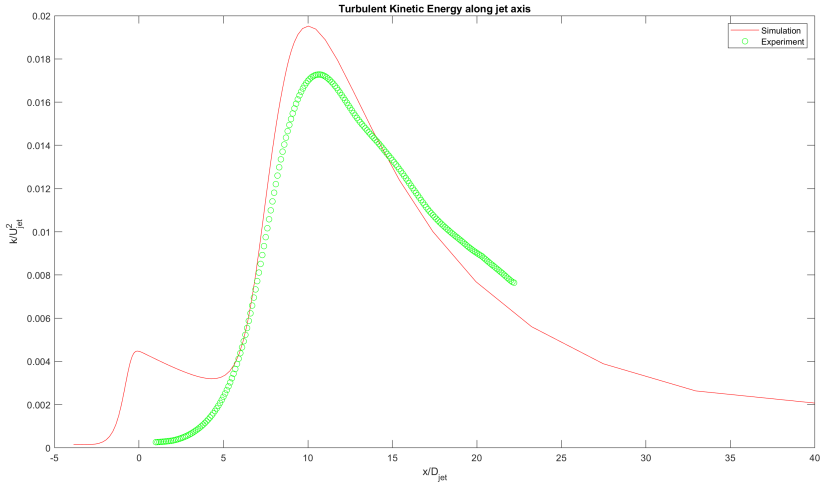

(b)

FIGURE 5 – Turbulent kinetic energy of axisymmetric jet

Along the axis the maximum turbulent kinetic energy can be seen to occur at $x/D = 10$, as per figure 5b. However, this location does not correspond with the global maximum

turbulent kinetic energy. In the equations for the turbulent kinetic energy in the $k-\epsilon$ model, the production term is given as $P_k = -\overline{u_i u_j}\frac{\partial \overline{U_i}}{\partial x_j}$. Both the turbulent fluctuations and the velocity gradient at are at a maximum in the shear layers, which itself is strongest at the nozzle exit before it begins to diffuse. Consequently, along fixed x/D positions the turbulent kinetic energy is highest slightly above the axis. This also correlates to the maximum turbulent kinetic energy on the axis occurring when the axis velocity experiences its largest velocity gradient as the shear layers intersect the axis.

After the maximum turbulent kinetic energy the jet enters a region of self similarity which is characterized by a linear spreading rate. To verify the jet has entered the self similar region the velocity profiles at different x/D values are normalized with respect to their axis velocity and the velocity half width, $\delta_{0.5}$. The half width is chosen to eliminate the intermittency of the jet boundaries.

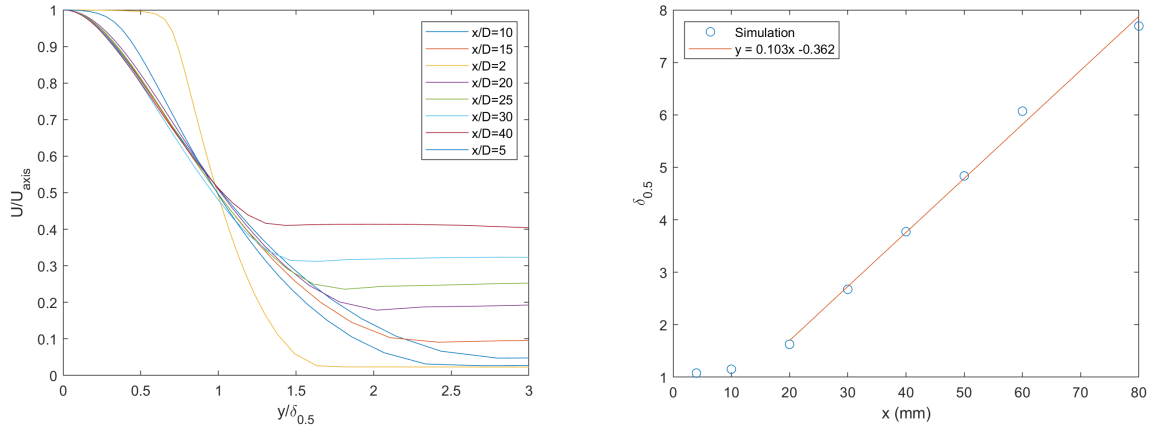

(a) (b)

FIGURE 6 – Self-similar region and linear spreading rate

From figure 6a the self similar region is confirmed to begin after $x/D = 10$. Performing a linear regression of the calculated $\delta_{0.5}$ in these stations leads to a numerical spreading rate of $\tau_e = 0.103$. The given range for experimental values is τ_e $0.086 - 0.095$, corresponding to an over estimation of $20\% - 8\%$ for the $k-\epsilon$ model, respectively.

On a more general basis, the simulation results can be compared with the provided experimental data. The velocity components, turbulent fluctuations, and turbulent kinetic energy are compared for three x/D stations below in figure 7. It can be seen that the simulation is able to better describe some characteristics of the jet more than others. The general shape of the profiles, as well as the location of the maximum values, are accurately predicted by the simulation. The axial velocity also displays minimal variation from the observed experimental values. In the case of V the simulation under predicts the magnitude at $x/D = 2$ and $x/D = 20$ along the profile. However, the simulation closely matches the

experiment at $x/D = 10$ while close to the axis, while over predicting the magnitude as the distance from the jet axis increases. Conversely, for the turbulent fluctuations and the turbulent kinetic energy, the simulation over predicts the values at $x/D = 2$ and $x/D = 10$, but under predicts the values at $x/D = 20$. There is a close relation between the shapes of the turbulent fluctuations and turbulent kinetic energy, likely due to the manner in which the former is calculated in the closure of the Navier-Stokes equation using the $k - \epsilon$ model.

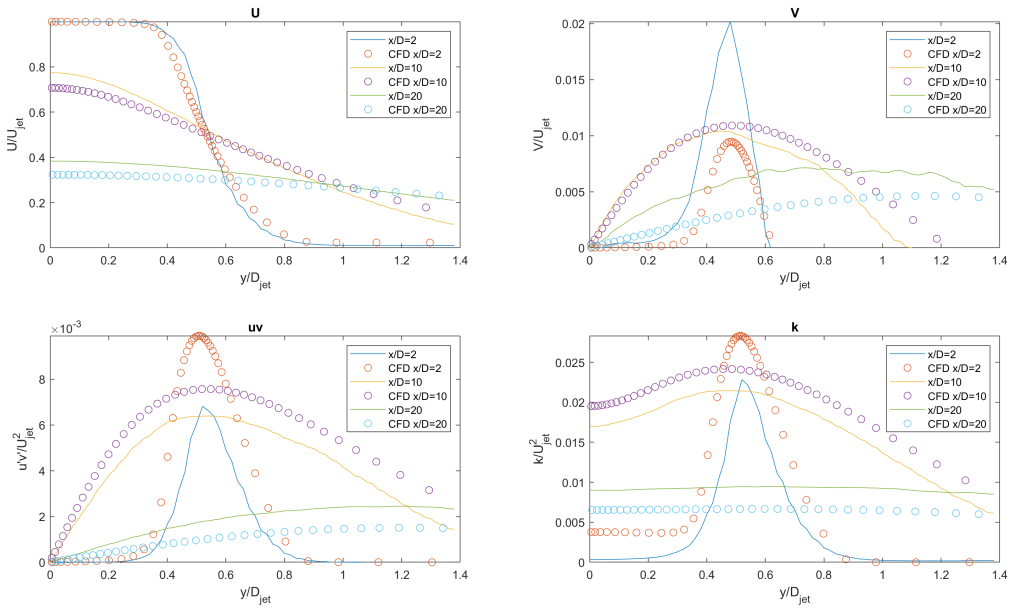

FIGURE 7 – Comparison between the experimental profiles and the simulated results at fixed x/D stations

A second simulation was performed modifying the model constant $C_{\epsilon 2}$ by increasing the value by 20%. This constant is related to the destruction of the dissipation rate, thus an increase in the constant means a quicker decay in the dissipation rate leading to a more energetic flow. A more energetic flow produces a greater degree of turbulence, and thus stronger shear layers.

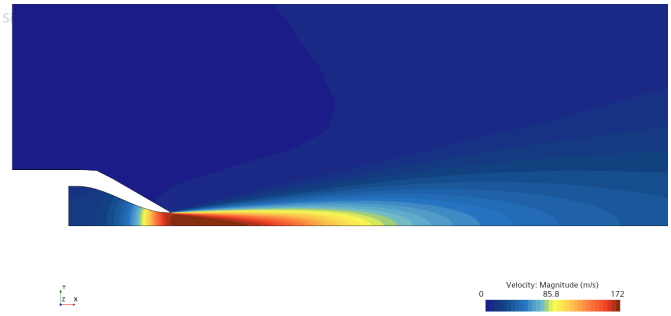

(a)

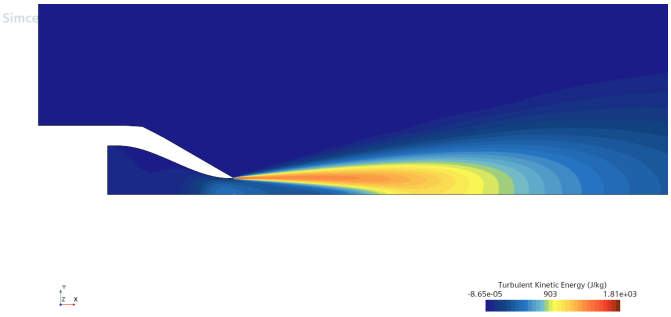

(b)

FIGURE 8 – Contours of velocity magnitude and turbulent kinetic energy for an increased $C_{\epsilon 2}$

The increase to $C_{\epsilon 2}$ caused a significant shortening of the potential core to an end position of $x/D = 2.5$. The increase also produced a higher value of max turbulent kinetic energy which occurred at an earlier station of $x/D = 6$ compared to the original simulation.

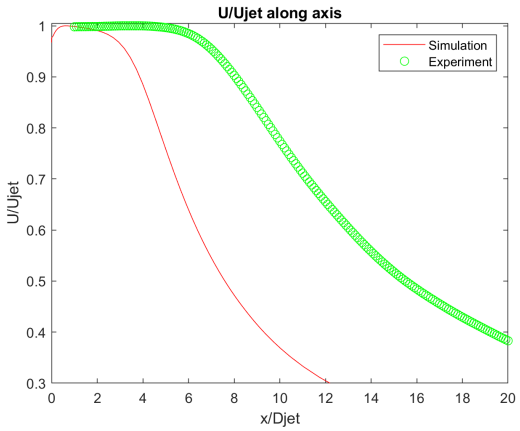

(a)

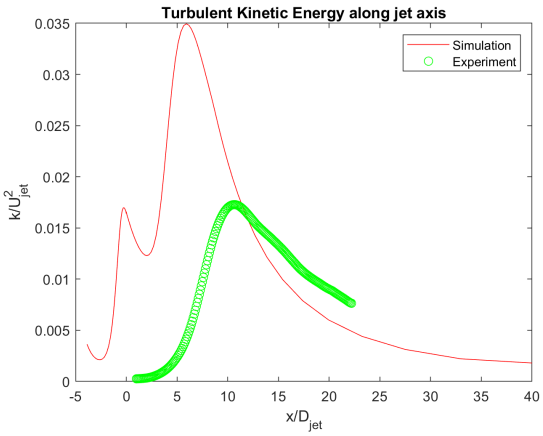

(b)

FIGURE 9 – Evolution of axial velocity and turbulent kinetic energy along the jet axis

The self similar region can be seen to begin from just after station $x/D = 5$, confirming the position from the turbulent kinetic energy plot. It is interesting to note that the self similarity seems to break down from $x/D = 30$ and the spreading rate increases drastically afterwards. It could be that the increase in kinetic energy of the system causes the jet to lose its coherence after this station and it begins to diffuse into the ambient flow. The calculated spreading rate over the self similar region is significantly higher than the original simulation, almost double the value.

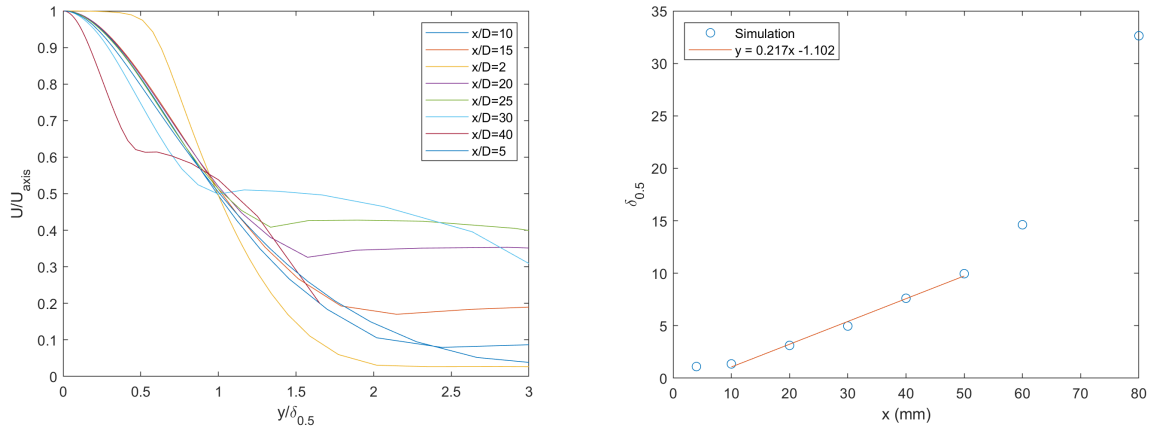

(a) (b)

FIGURE 10 – Self-similar region and linear spreading rate

The third simulation consisted of increasing the initial turbulent kinetic energy of the jet. This was realized by increasing the turbulence intensity of the nozzle inlet by factor of five. The expected effect was similar to that of the previous simulation.

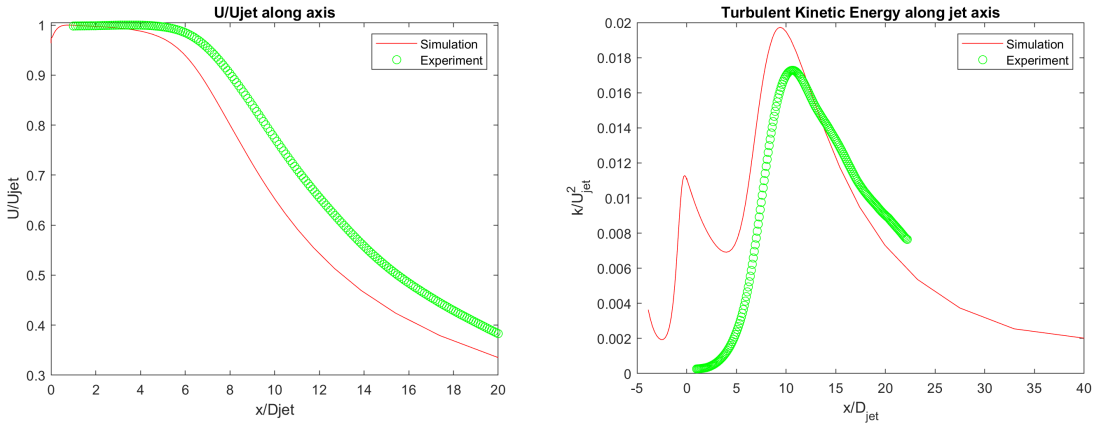

(a) (b)

FIGURE 11 – Evolution of axial velocity and turbulent kinetic energy along the jet axis

As seen from the above figures the potential core was shortened and an earlier maximum turbulent kinetic energy were experienced, compared to the initial simulation. However, the changes were not as drastic as the previous case. For the self similarity, the jet displays a spreading rate in close agreement with the original value. This is not unexpected, as the model was unchanged, the jet parameters were simply increased slightly.

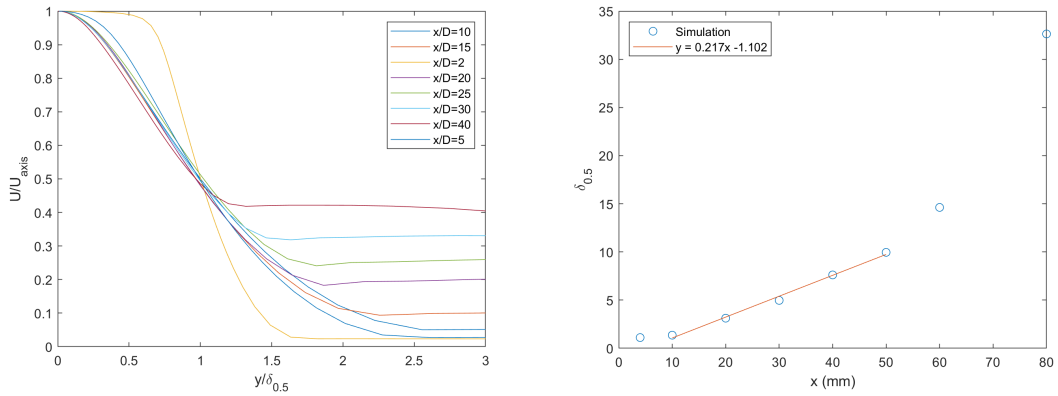

(a) (b)

FIGURE 12 – Self-similar region and linear spreading rate

A subsequent investigation was made regarding the choice of turbulent model. In place of the $k - \epsilon$ model, the Spalart-Allmaras (SA) model was utilized. Being a one equation model, SA does not compute the turbulent kinetic energy thus a comparison between models cannot be made on this fact. However, the models can still be compared on the basis of the potential core and the self similar region.

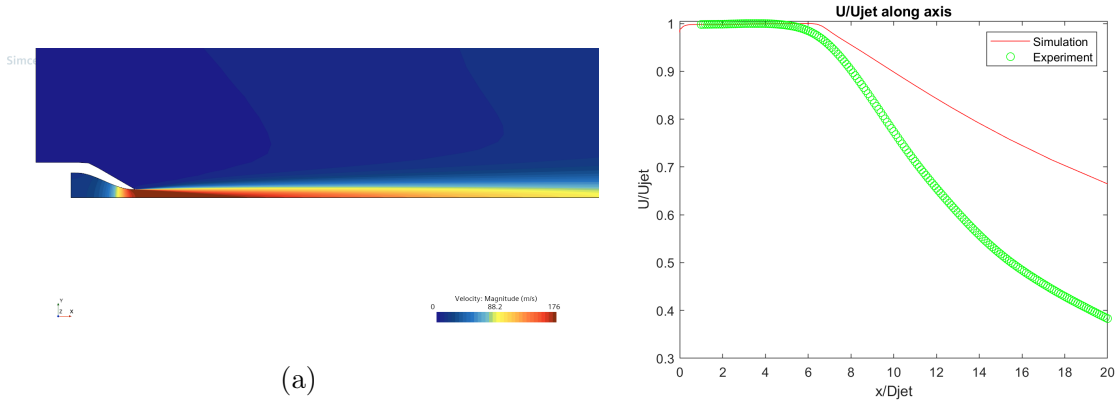

(a) (b)

FIGURE 13 – Velocity contour produced using Spalart-Allmaras model, and the velocity evolution along the jet axis

The SA model predicted a longer potential core, terminating at $x/D = 7$. However, the greatest difference between the models is the spreading rate. The self similar region begins at approximately the same x/D station, however the SA model vastly under predicts the spreading rate, returning a value almost one quarter of that produced by the $k - \epsilon$ model. Comparing between the original simulation and the experimental results, it is obvious that the SA model is not suited to the modelling of turbulent jet flows.

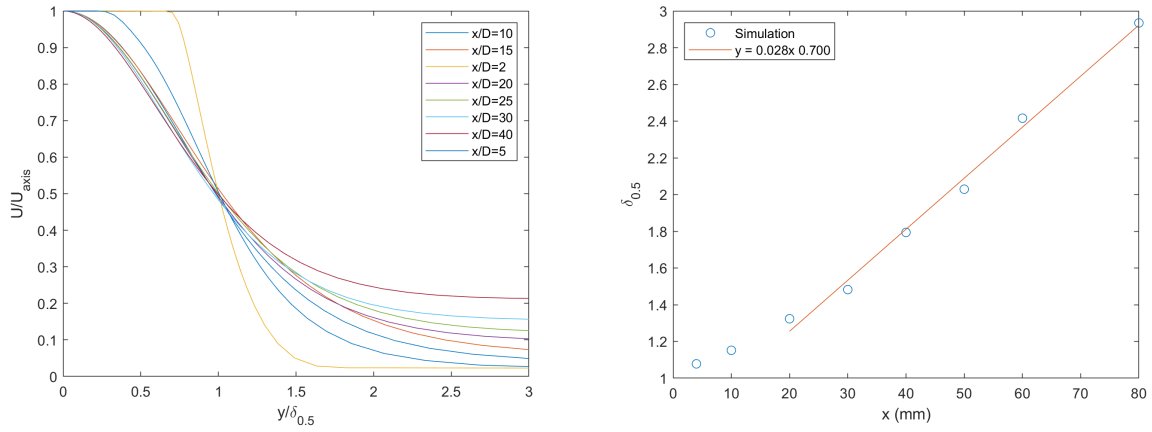

(a) (b)

FIGURE 14 – Self-similar region and linear spreading rate

As described at the beginning of this section, the jet analysed up to this point was a round axisymmetric jet allowing for a 2D simplification. Aside from a round jet, a jet whose width is sufficiently larger than its height can also be simplified as a 2D plane jet. A simulation was performed on this case, and the following analysis will highlight the differences between these two 2D jets.

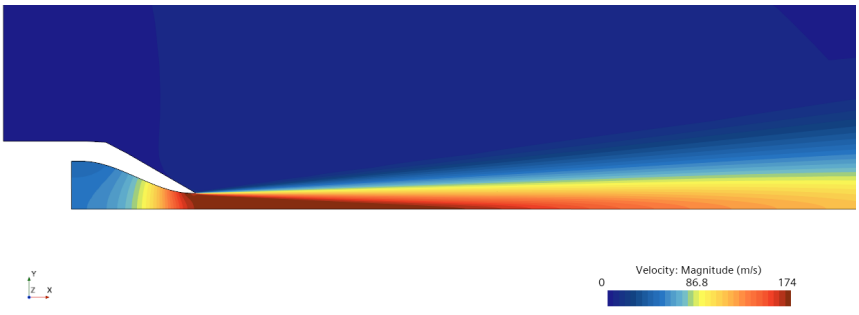

FIGURE 15 – Velocity contour of the simulated plane jet

The most obvious difference between the round and plane jet is the lengths of the potential core and adaptation zone. As seen in figure 16, the potential core ends around

$x/D = 8$, a 33% increase in length compared to the round jet. Furthermore, the termination of the potential core is less distinct, with a shallower velocity gradient along the jet axis. The relative length of the adaptation zone is also increased for the plane jet. Terminating at $x/D = 17$ the zone is approximately equal in length to the potential core, unlike the plane jet case, where it was only about 67% of the core. In the case of the plane jet, there is also a lower overall magnitude to the turbulent kinetic energy.

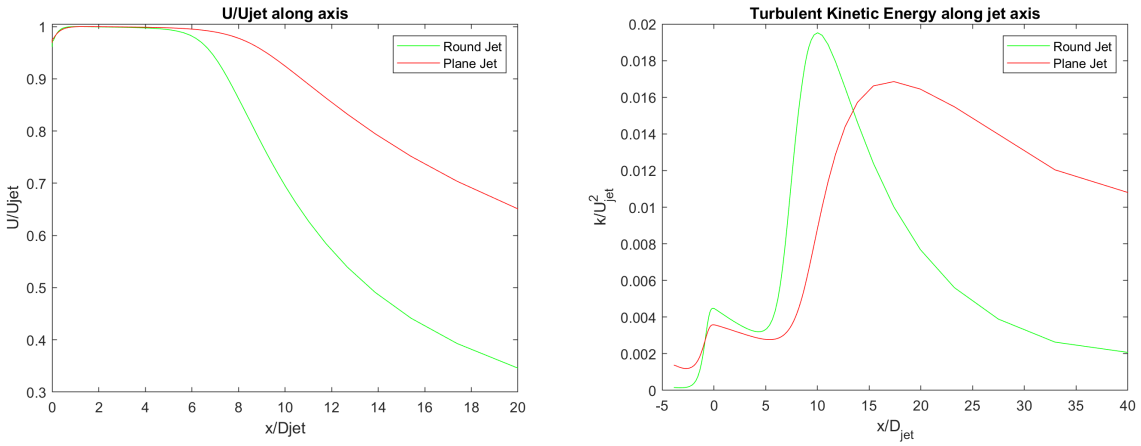

(a) (b)

FIGURE 16 – Evolution of axial velocity and turbulent kinetic energy along the jet mid-plane

In the case of the round jet, the axisymmetry means that the jet is able to produce a uniform expansion rate about the axis. In the case of the plane jet, expansion would not be possible in the direction of the jet width. Thus, it would be expected that this restriction would produce a larger spreading rate in the direction perpendicular to the jet width. However, this was not the case observed in the simulation. Firstly, from the extended length of the adaptation zone, the self-similar region of the plane jet begins later than the round jet. In this self-similar region the plane jet displays a spreading rate approximately 6% below that of the round jet.

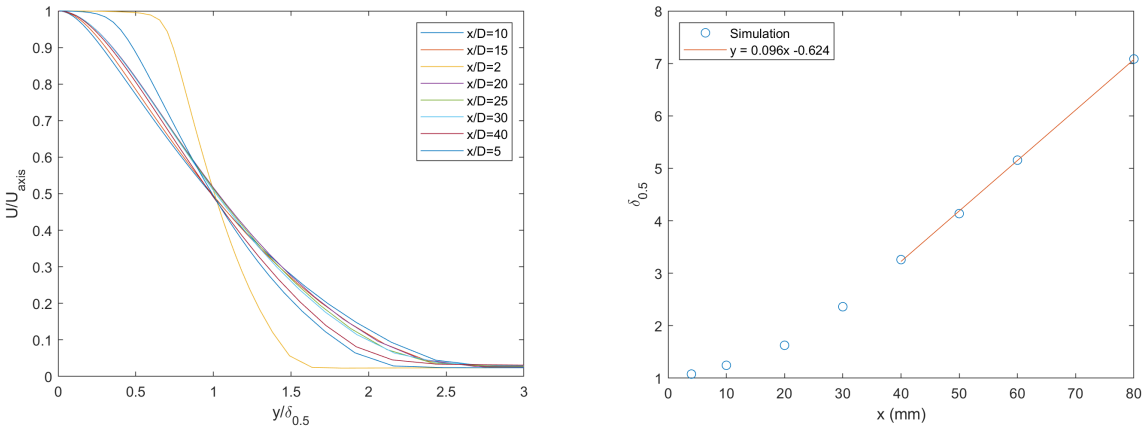

(a) (b)

FIGURE 17 – Self-similar region and linear spreading rate

Turbulent boundary layer on a NACA 4412 airfoil

The turbulent flow over a NACA4412 airfoil at chord-based Reynolds number (Re_c) of 1.52×10^6, Mach number (M) of 0.09, and angle of attack (α) equals to 13.87° has been considered.The fluid field has been resolved by employing the Reynolds averaged incompressible 2D N-S equations closed with the $k-\omega$ SST turbulent model with correction for low-Reynolds flows and the equations are solved in StarCCM+ with 2^{nd} order accuracy in space and time. The computational domain (449*129) is defined in a way that the external boundary of the domain, 50c away from airfoil, doesn't influence flow development in near-airfoil region.

To validate the correctness of the turbulence model version, the y^+ parameter has been plotted. It is noteworthy that the y^+ criterion is contingent on the flow conditions. Thus, meaningful verification is only applicable after obtaining an initial solution with a suitably chosen first cell size. However, from the Fig.18 it can be said that y^+ is consistently below 1. Using a low Re model down to the wall will only provide accurate results if the first cell is smaller than $y^+ = 5$. The reason is the viscous sub-layer can be done using linear law ($\bar{U} = (y^+)$), which is only applicable for $y^+ \leq 5$.

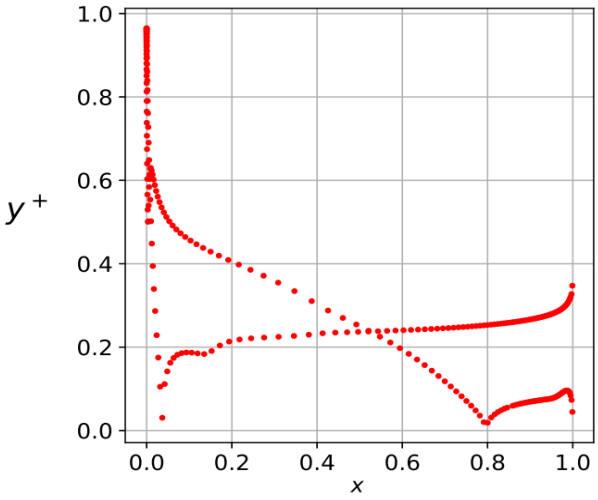

FIGURE 18 – y^+ value on both suction and pressure side

The RANS simulation results closely approximate the experimental data with a slight margin of error (see Table1). While anticipated to diverge, the pressure and friction coefficients exhibit a satisfactory concurrence at the trailing edge (see Fig.19). This alignment occurs as the flow departs unsteadily, indicating an adept depiction of the separation point.

	Mean C_l	Mean C_d	Mean C_d(viscous)	Mean C_d(pressure)
EXP	1.616	0.0311	0.00687	0.0242
CFD	1.624	0.0306	0.00694	0.0237
Variation(%)	-0.5	1.6		

TABLE 1 – Comparison of Exp and CFD (C_l, C_d)

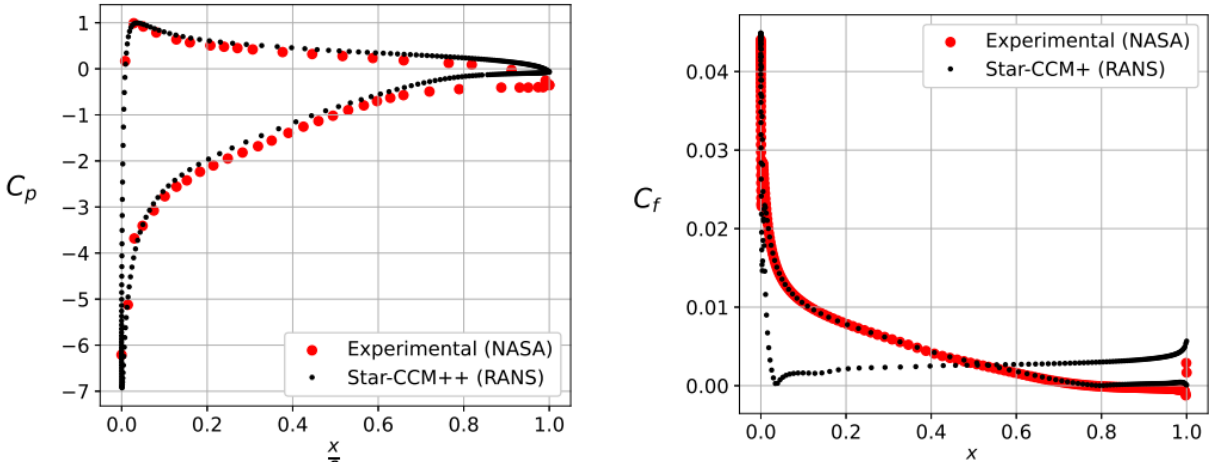

(a) Pressure coefficient

(b) Skin Friction coefficient

FIGURE 19 – Comparison of C_p and C_f of exp/cfd

An investigation into various velocity profiles has been carried out. Specifically, six line probes were positioned along the suction side at $x/c = [0.6753, 0.7308, 0.7863, 0.8418, 0.8973, 0.9528]$, in such a way that these line probes are positioned across the separation bubble at the trailing edge. At each location, the exported values of ($\overline{U}$, $\overline{V}$, $\overline{u'v'}$) are examined and compared with experimental data from NASA. Despite the observable agreement between the numerical analysis results and experimental data for $\overline{U}$ and $\overline{V}$, the numerical simulation exhibits an underestimation of turbulence production compared to the experimental results.

According to the velocity profile, (see Fig.20a) the initiation of instability is accurately captured. As the separation develops, the stream-wise velocity correctly reverse it's direction due to the re-circulation zone. The crosswise velocity (see Fig.20b) demonstrates acceptable conformity before separation. However, there is a numerical underestimation near the wall as the crosswise velocity undergoes a change in sign due to local swirling.

The double correlation term (See Fig.21) is qualitatively captured, consistently appearing negative. Experimental results have indeed validated the correlation between streamwise and crosswise velocity fluctuations, manifesting as a turbulent diffusion mechanism mathematically represented by a negative averaged product, specifically the Reynolds stress

$\overline{u'v'}$, which must be negative. The negative correlation is connected to the blockage effect near the wall, as the decreasing effectiveness of swirling eddies leads to an approach of zero Reynolds stress and, subsequently, a near-zero turbulent diffusion. Despite this, the overall portrayal consistently falls short at each location, signifying a local underestimation of turbulent kinetic energy production and the oscillations in stream-wise velocity.

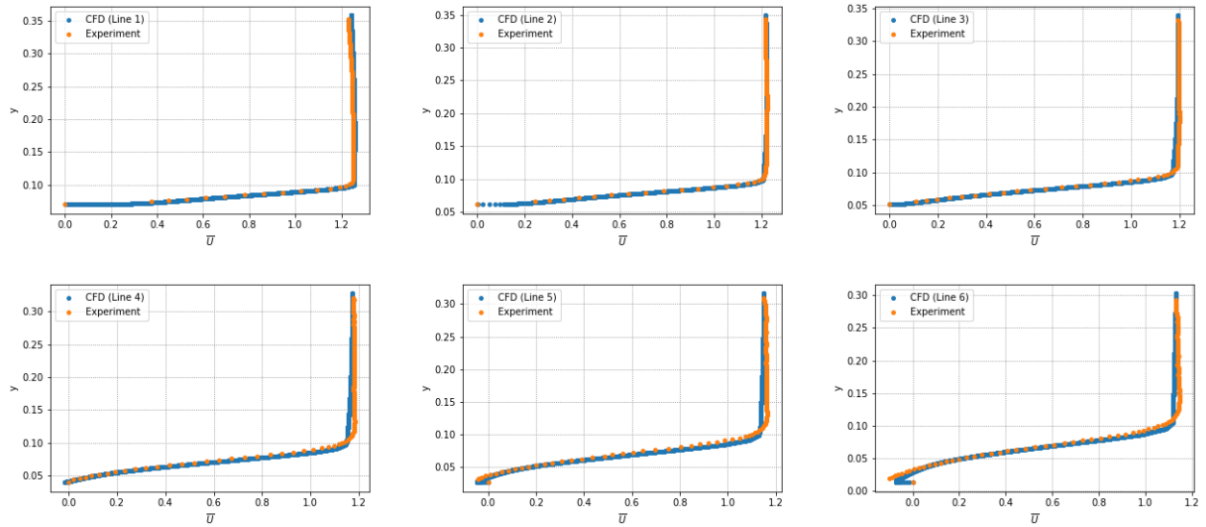

(a) y vs $\overline{U}$

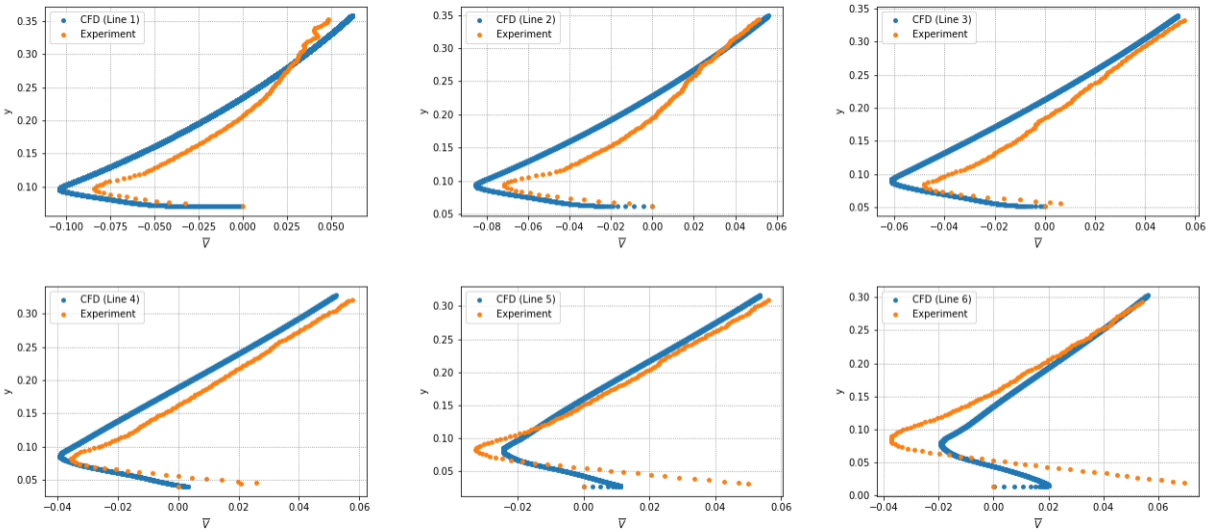

(b) y vs $\overline{V}$

FIGURE 20 – Comparison of (a) $\overline{U}$, (b) $\overline{V}$ of exp/cfd from the probes data.

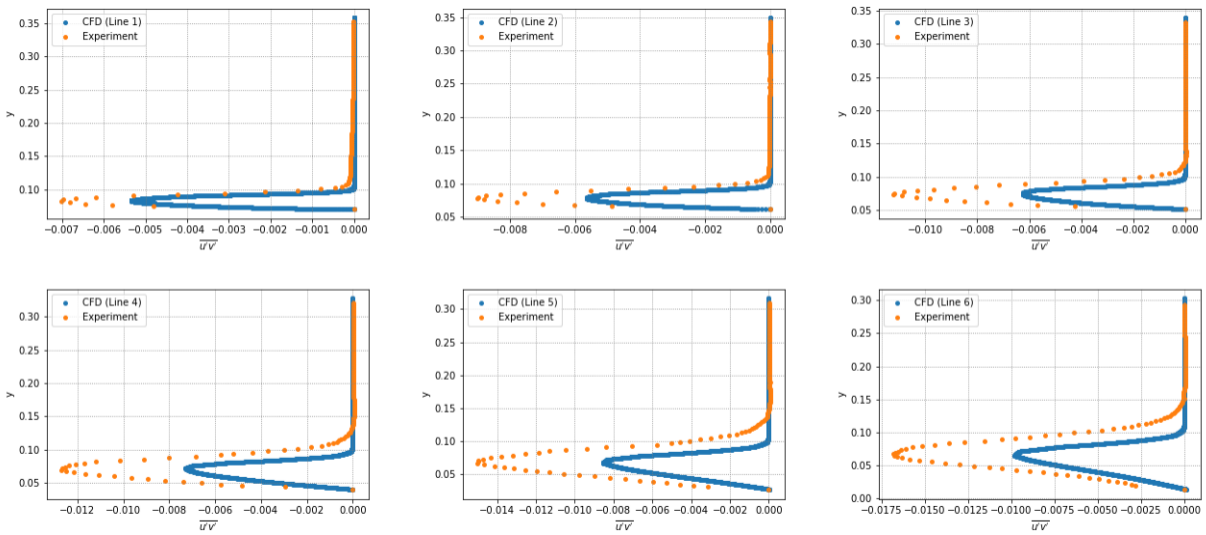

FIGURE 21 – Comparison of $\overline{u'v'}$ of exp/cfd from the probes data.

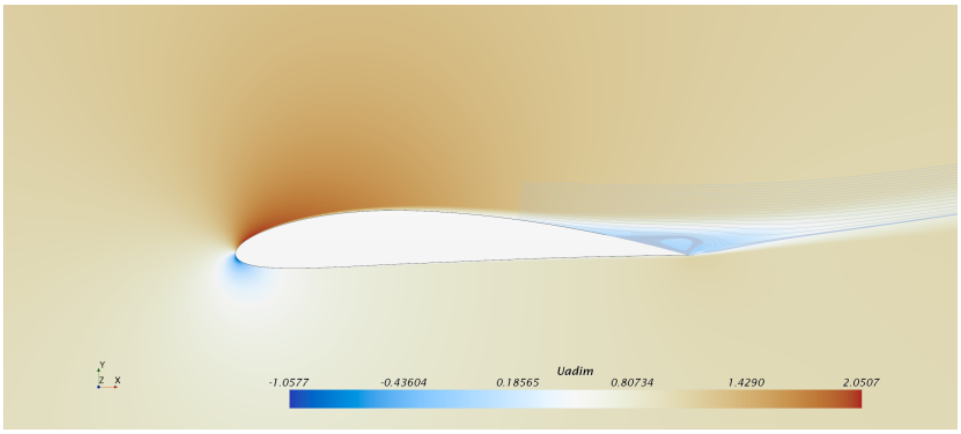

FIGURE 22 – Velocity contour with streamlines at separation region.

As depicted in the illustration (see Fig.23) for the three-line probes at x/c equal to 0.3 on the suction side, 0.5 on the pressure side, and 0.6753 on the suction side, the viscous sub-layer exhibits similar trends, which is $U^+ = y^+$. However, variations are anticipated in the characteristics of the wake zones. It is worth mentioning that the numerical probes do not extend to the physical wall, resulting in non-zero velocity at the initial point of each probe.

The extension of the log layer is quite marked at $x/c = 0.3$ (suction side) and $x/c = 0.5$ (pressure side) far upstream, or in absence of separation onset. The increased turbulent Reynolds number also contributes to the stretching of the log layer. Furthermore, the

momentum thickness-based Reynolds number R_θ is expected to vary, notably with a higher value at the latter location, explaining the leftward stretching of the velocity profile. The probe at $x/c = 0.6753$ is in the separation zone shortening the overlap region. Indeed, because of the re-circulation region, characterized by nearly zero local velocity, the local Reynolds number is consistently low, hindering the formation of the log layer.

Nevertheless, when determining the conclusion of the logarithmic region based on the qualitative linear trend observed on a semi-log scale, it is noted that the log region extends from $[60, 100]$ for $x/c = 0.3$, $[70, 110]$ for $x/c = 0.5$ and $[80, 100]$ for $x/c = 0.6753$.

Furthermore, another distinction is evident in the wake region, influenced by the local pressure gradient. In particular, the incoming flow at the trailing edge experiences a significant pressure variation due to the curvature of the airfoil. Moreover, for the computation of the wake parameter, the vertical distance from the log region line ($U^+ = \ln(y^+/0.41) + 5.2$) to the curve in the wake region is equated to $2\pi\kappa$. Consequently, the wake parameter is approximated to be : 0.615 at $x/c = 0.3$, 0.410 at $x/c = 0.5$ and 4.10 at $x/c = 0.6753$.

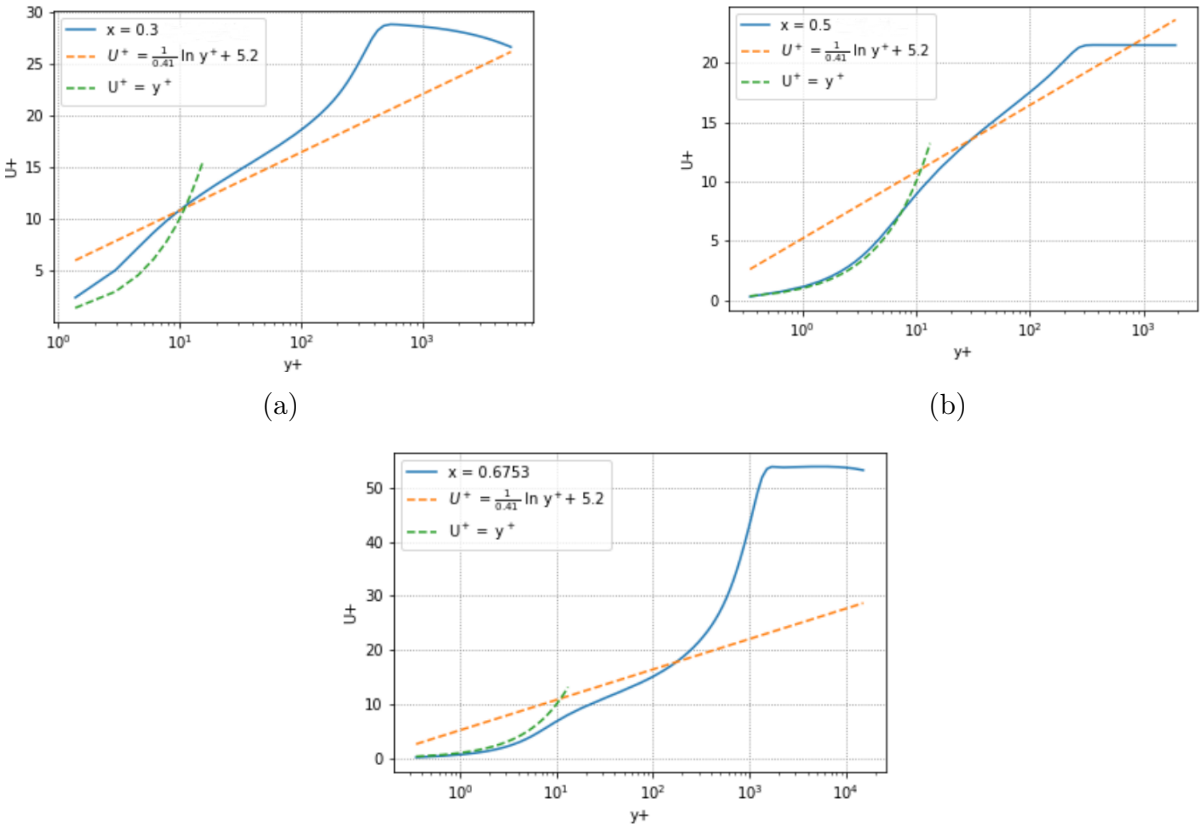

FIGURE 23 – Velocity profiles for three line probes. (a) $x/c = 0.3$, (b) $x/c = 0.5$, (c)$x/c = 0.6753$

Evaluating the quantity $\frac{u'v'}{k}$ provides a means to confirm the prescribed turbulence diffusivity coefficient in the transport equation for the $k-\varepsilon$ model.

$$\begin{aligned} \nu_t &= \frac{C_\mu k^2}{\varepsilon} \\ \overline{\mu_t} = \frac{\nu_t}{\varepsilon/k} &= \frac{u'v'}{k^2} \quad ; u'v' < 0 \\ \frac{u'v'}{k} = 0.3 \quad &\Rightarrow \quad C_\mu = 0.09 \end{aligned} \tag{1}$$

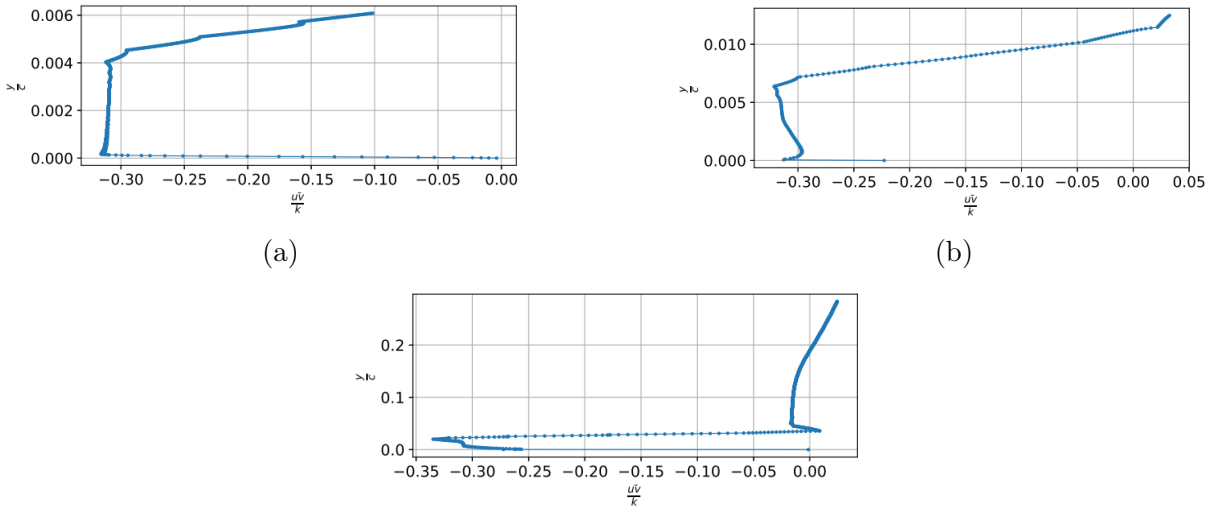

FIGURE 24 – Comparison of $\frac{u'v'}{k}$ (cfd results) at (a) $x/c = 0.3$, (b) $x/c = 0.5$, (c)$x/c = 0.6753$

The Reynolds stress is typically $u'v' < 0$, at each cross-section because of the blockage effect in the boundary layer. Whereas, at the trailing edge (see Fig.24c) there is a region where the $u'v'$ term is strengthened due to re-circulation owing to presence of separation bubble. Concerning the energy distribution, within a small segment of the boundary layer, the stream-wise oscillations receive significant energy input from the gradient of the mean flow. Specifically, the energy being generated is redistributed among the cross-wise and span-wise components of the Reynolds stress through the pressure strain tensor.

While the probes are not directly placed on the wall, hindering them from capturing the trend in extremely close proximity to the wall, it is evident that just above the viscous sub-layer, turbulent kinetic energy production reaches its maximum where turbulent diffusion is maximized and then drops because of increased viscous dissipation at the wall.

Across the boundary-layer thickness, the total stress comprises both viscous and turbulent stress, and this sum remains constant (eqn.(2)). In the viscous sub-layer, the total stress τ_{tot} is approx equal to τ_ν, given that the Reynolds stress tends toward zero, with viscosity diffusion playing a predominant role. (see Fig.25) With increasing distance from the wall, turbulent diffusion takes precedence, causing the total stress to disintegrate into turbulent stress.

$$\nu\frac{\partial U}{\partial y} - u'v' = \tau_t + \tau_\nu = \tau_{\text{tot}} = \nu\frac{\partial U}{\partial y}\Big|_{\text{wall}} = \rho u^2 \tag{2}$$

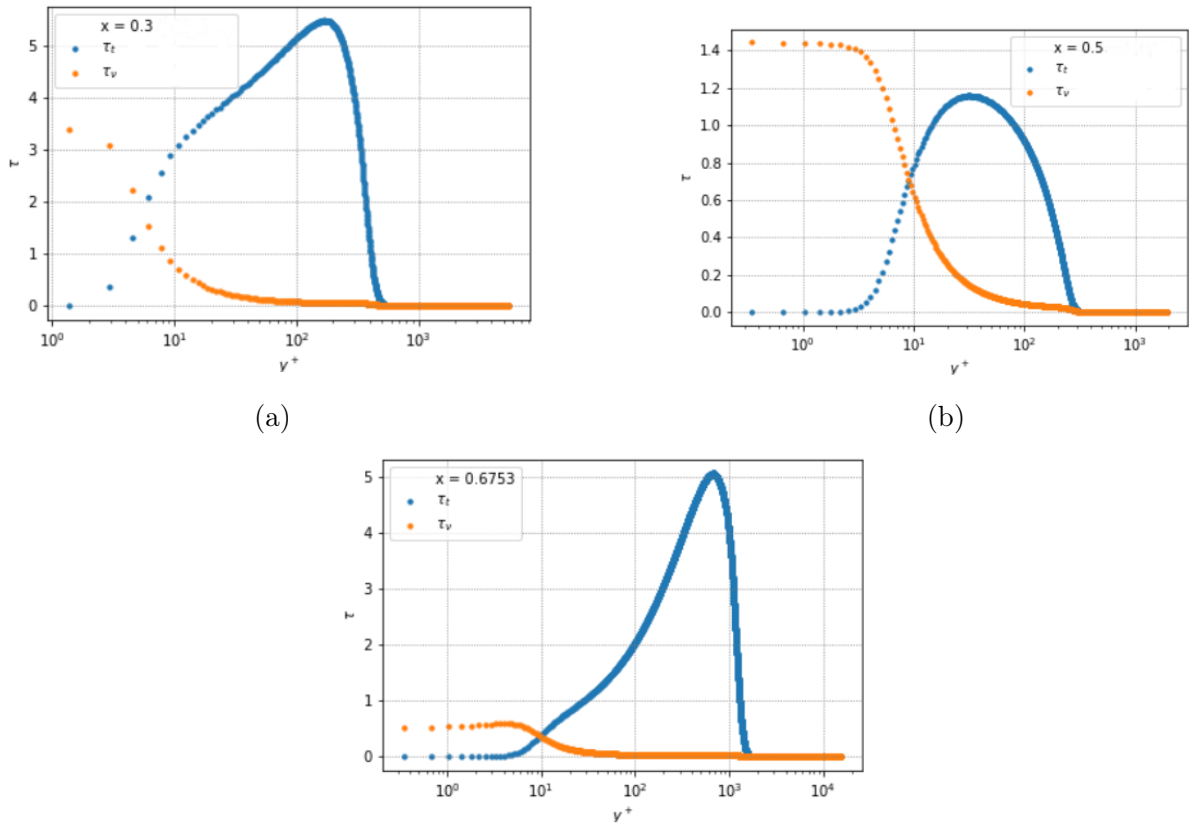

(a) (b)

(c)

FIGURE 25 – Comparison of τ_v, τ_t (cfd results) at (a) $x/c = 0.3$, (b) $x/c = 0.5$, (c)$x/c = 0.6753$

Conclusion

Throughout the previous sections, the physics and efficacy of turbulent RANS models with respect to experimental flows was investigated. In the case of an axisymmetric turbulent free jet, the $k-\epsilon$ model was able to accurately capture the general shape of a turbulent jet. In terms of the magnitudes calculated, the $k-\epsilon$ model had a tendency to over predict values. In the case of the spreading rate there was a significant over prediction averaging around 14% when compared to the experimental values.

An investigation into alternative turbulence models demonstrated that the Spalart-Allmaras model was significantly worse in simulating the jet physics ; an extended potential core and a vastly under expanded jet characterized the Spalart-Almaras jet.

The turbulent boundary layer resolution over a NACA profile indicates consistent concordance. Notably, the low-Reynolds version of the $k-\omega$ SST model successfully captures the velocity profile on both the suction and pressure sides. The pressure distribution, lift, drag, and identification of separation onset are also accurately determined with minimal errors. However, the $k-\omega$ SST model is not well-suited to accurately solve the energy distribution and Reynolds stress.